

Induced polarization tomography applied to the detection and the monitoring of leaks in embankments

F. Abdulsamad, A. Revil, A. Soueid Ahmed, A. Coperey, M. Karaoulis, Sylvie Nicaise, Laurent Peyras

▶ **To cite this version:**

F. Abdulsamad, A. Revil, A. Soueid Ahmed, A. Coperey, M. Karaoulis, et al.. Induced polarization tomography applied to the detection and the monitoring of leaks in embankments. Engineering Geology, 2019, 254, pp.89-101. 10.1016/j.enggeo.2019.04.001 . hal-02324239

HAL Id: hal-02324239
https://hal.science/hal-02324239

Submitted on 23 Nov 2020

HAL is a multi-disciplinary open access archive for the deposit and dissemination of scientific research documents, whether they are published or not. The documents may come from teaching and research institutions in France or abroad, or from public or private research centers.

L'archive ouverte pluridisciplinaire **HAL**, est destinée au dépôt et à la diffusion de documents scientifiques de niveau recherche, publiés ou non, émanant des établissements d'enseignement et de recherche français ou étrangers, des laboratoires publics ou privés.

Engineering Geology 254 (2019) 89–101

Contents lists available at ScienceDirect

Engineering Geology

journal homepage: www.elsevier.com/locate/enggeo

Induced polarization tomography applied to the detection and the monitoring of leaks in embankments

F. Abdulsamad[a], A. Revil[a,*], A. Soueid Ahmed[a], A. Coperey[a], M. Karaoulis[b], S. Nicaise[c], L. Peyras[c]

[a] Université Grenoble Alpes, Université Savoie Mont Blanc, CNRS, IRD, IFSTTAR, ISTerre, 38000 Grenoble, France
[b] Deltares, Utrecht, Netherlands
[c] IRSTEA, Aix-en-Provence, France

ABSTRACT

During an induced polarization survey, both electrical conductivity and chargeability can be imaged. Recent petrophysical models have been developed to provide a consistent picture of these two parameters in terms of water and clay contents of soils. We test the ability of this method at a test site in which a controlled artificial leakage can be generated in an embankment surrounding an experimental basin. 3D tomography of the conductivity and normalized chargeability are performed during such a controlled leakage. Conductivity and induced polarization measurements were also performed on a core sample from the site. The sample was also characterized in terms of porosity and cation exchange capacity. Combining the 3D survey and these laboratory measurements, a 3D tomogram of the relative variation in water content (before leakage and during leakage) was estimated. It clearly exhibits the ground water flow path through the embankment from the outlet of the tube used to generate the leak to the bottom of the embankment. In addition, a self-potential survey was performed over the zone of leakage. This survey evidences also the projection of the ground water flow path over the ground surface. Both methods are found to provide a consistent picture. A 2.5D time lapse tomography of the electrical conductivity and normalized chargeability was also performed and evidences the position of the preferential flow paths below the profile. These results confirm the ability and efficiency of induced polarization to provide reliable information pertaining to the detection of leakages in dams and embankments.

1. Introduction

Embankment dams and dikes can be weakened by internal erosion and suffusion phenomena due to preferential flow paths and this ongoing weakening can cause their failure (e.g., Foster et al., 2000; Peyras et al., 2008). Early warning associated with the concentration of flow paths in an embankment is therefore an important task to prevent its failure. On one hand, traditional geotechnical technics (e.g., cone penetration test and/or standard penetration tests) have limitations related to cost-effectiveness and the perturbation on the structures themselves (e.g., Fauchard and Mériaux, 2007; Cardarelli et al., 2014). Temperature measurements using fiber optics can be used to evaluate leakages (Beck et al., 2010; Khan et al., 2014), but such approaches are unfortunately intrusive. On the other hand, geophysical methods can provide fast and non-intrusive 3D and 4D tomograms of leakages using a variety of techniques (e.g., Rittgers et al., 2013; Ikard et al., 2015).

Different geophysical methods can be used to detect preferential flow paths in embankment dams and dikes including ground penetrating radar, passive and active seismic methods (Himi et al., 2018), and geoelectrical (galvanometric) methods including the self-potential method (Al-Saigh et al., 1994) and electrical conductivity and induced polarization methods (e.g., Martínez-Moreno et al., 2018). Ground Penetrating Radar (GPR) constitutes a fast and reliable method for shallow investigations. However, the so-called skin depth of GPR (i.e., the depth of penetration of the electromagnetic waves at a given frequency) can be very small in conductive media, such as, for instance, in presence of clays (Di Prinzio et al., 2010). Geoelectrical (galvanometric) methods (electrical conductivity, induced polarization, and self-potential) do not suffer such a limitation (Mendonça, 2008). A detailed description of the electrical conductivity and induced polarization method can be found for instance in Binley and Kemna (2005) and Revil et al. (2012). In the case of dikes and dams, electrical conductivity tomography is known to provide important information for the assessment of preferential flow paths (Perri et al., 2014; Cardarelli et al., 2014; Fargier et al., 2014). However electrical conductivity tomography is related to the water content and not to the flow of the ground water. In addition, electrical conductivity can be hardly used as a stand-alone technique. Indeed, two contributions control the electrical conductivity of porous soils. One associated with the conduction in the bulk pore space and one associated with conduction in the electrical double layer coating the surface of the grains. This second contribution is called surface conductivity and is especially strong in clay-rich materials and/or at low pore water

* Corresponding author.
E-mail addresses: feras.abdul-samad@univ-smb.fr (F. Abdulsamad), andre.revil@univ-smb.fr (A. Revil), abdellahi.soueid-ahmed@univ-smb.fr (A. Soueid Ahmed), antoine.coperey@gmail.com (A. Coperey), Marios.Karaoulis@deltares.nl (M. Karaoulis), sylvie.nicaise@irstea.fr (S. Nicaise), laurent.peyras@irstea.fr (L. Peyras).

https://doi.org/10.1016/j.enggeo.2019.04.001
Received 4 December 2018; Received in revised form 1 April 2019; Accepted 2 April 2019
Available online 11 April 2019
0013-7952/ © 2019 Elsevier B.V. All rights reserved.

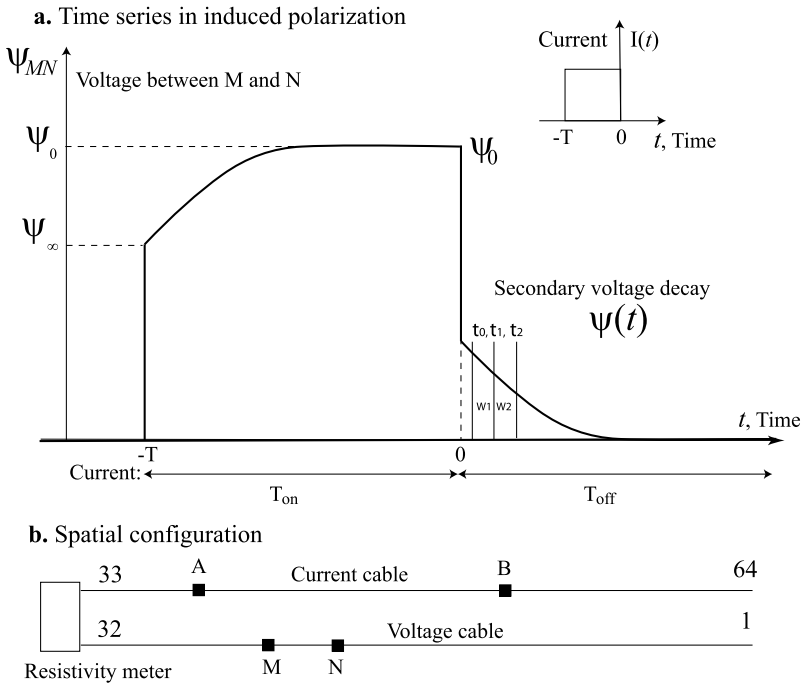


Fig. 1. Time-domain induced polarization data. (a) The primary current injected in the ground between electrodes A and B corresponds to a box signal of period T. The potential difference between the voltage electrodes M and N is the sum of a primary voltage ψ_∞ and a secondary voltage ψ_0–ψ_∞. Once the primary current is shut down (for $t > 0$), only the secondary voltage persists, decaying over time while the charge carriers are coming back to their equilibrium position. This decaying secondary voltage is measured into windows (W_1, W_2, etc.) separated by characteristic times (t_0, t_1, t_2, …). The partial chargeabilities are determined for each of these windows by integrating the secondary voltage over time. T_{on} and T_{off} denote the time of current injection and time for potential decay measurement, respectively. The time t_0 is a delay time before starting the partial chargeability measurement (dead time). (b) Spatial configuration for the induced polarization measurements. We used two sets of 32 electrodes for the current and voltage electrodes. These two sets are located on two distinct cables to minimize spurious electromagnetic effects and electrode polarization effects. The numbers 1 to 64 correspond to the labels of the electrodes in the protocol.

salinity even for clean sands (Revil et al., 2014). Electrical conductivity tomography cannot be used to separate the bulk conductivity from the surface conductivity. This point is crucial as discussed below since bulk and surface conductivities have very different dependencies with the pore water content. Induced polarization can be used to separate the two contributions of electrical conductivity. Before discussing induced polarization in more details, it is worth mentioning another technique called magneto-resistivity, which can be used to track preferential flow paths as discussed in details in Jessop et al. (2018). Another method, directly related to the flow of the ground water, is the self-potential technique (Lapenna et al., 2000; Bolève et al., 2009; Revil et al., 2005). This method is a passive geoelectrical method in which the flow of water generates its own source current distribution, the streaming current, which in turn generates an electrical potential anomaly at the ground surface. This electrical potential anomaly can be sampled at the ground surface with a pair of non-polarizing electrodes (one used as a reference) and high input-impedance voltmeter. This method has been broadly used for the detection of seepages in embankments (e.g., Nzumotcha-Tchoumkam et al., 2010). However other sources of current exist in the subsurface (e.g., associated with the corrosion of metallic bars and ores, Mendonça, 2008) and can make the interpretation of self-potential signals more difficult (Revil et al., 2012).

We are interested to use the induced polarization method to detect leaks. Induced polarization measures the ability of rocks and soils to store reversibly electrical charges under the influence of an external electrical field and the relaxation time required by these charges to come back to equilibrium once the applied electrical field is suppressed. Induced polarization has a very long history in geophysics with early development done for ore body prospection (Vinegar and Waxman, 1984; Titov et al., 2010). Great progresses have been recently done regarding the underlying petrophysics of induced polarization and a model called the dynamic Stern layer polarization model seems to explain laboratory data for a broad range of porous media and environmental conditions (see details in Revil and Florsch, 2010; Revil, 2013). In parallel, Soueid Ahmed et al. (2018) recently developed an inversion code (ECT-3D) to invert electrical conductivity tomography with complex topography. This work was completed by Soueid Ahmed and Revil (2018) who developed a 3D joint inversion package for electrical conductivity and induced polarization tomography.

In this paper, we develop a field experiment over an experimental basin using induced polarization tomography. The aim of this study is to provide a way to analyze the advantage of using induced polarization to detect leaks in such infrastructures. The key questions we address are the following (1) Can we use a time-lapse induced polarization survey to determine soil moisture changes associated with an ongoing leakage? (2) Can we combine induced polarization tomography and the dynamic Stern layer model to image the change of the water content in an embankment?

2. Induced polarization

2.1. Principle of the measurements

Induced polarization investigates the ability of porous materials to store reversibly electric charges under the action of an external (primary) electrical field (Vinegar and Waxman, 1984). Induced polarization measurements can be performed in time-domain or frequency domain (the so-called spectral induced polarization method). In time-domain induced polarization, we measure the secondary voltage decay after the primary current (and primary electrical field) is shut down (Fig. 1). In frequency-domain induced polarization, the amplitude of the electrical field and current and their phase shift are used to obtain a frequency-dependent impedance, which is, in turn, converted into a complex conductivity using a geometrical factor that depends on the geometry of the electrode array and boundary conditions. The real part (in-phase component) of this complex conductivity denotes the ability of a porous material to conduct current and is therefore associated with the electro-migration of the charge carriers. The imaginary part (quadrature component) corresponds *stricto sensu* to the polarization of the material, i.e. to the ability of the material to store reversibly electrical charges under the action of the primary (applied) electrical filed (Titov et al., 2010; Revil and Florsch, 2010).

The concept being time-domain induced polarization data is sketched in Fig. 1. A box current is injected between two electrodes A and B with a period T. The resulting electrical potential distribution is sampled between two electrodes M and N. When the primary current is shut

down, the secondary current decays over time (Fig. 1). This decay expresses the fact that the stored electrical charges comes back to their statistical equilibrium position by electro-diffusion. The secondary voltage decay can be densely sampled in order to perform full waveform inversion. That said, when we are simply interested to image the chargeability, it is enough to sample the voltage curve over a series of windows (typically 10 windows are enough) Then, the polarization data are formed by partial (apparent) chargeabilities (expressed in ms). These partial chargeabilities M_i are obtained by integrating the secondary voltage decay between times t_i and t_{i+1} ($t = 0$ s corresponds to the time of the shutdown of the primary current, Fig. 1)

$$M_i = \frac{1}{\psi_0}\int_{t_i}^{t_{i+1}} \psi(t)dt. \tag{1}$$

In Eq. (1), ψ_0 denote the potential difference between the electrodes M and N just before the shutdown of the primary current, $\psi(t)$ denote the secondary voltage decay curve (Fig. 1a), $t_{i+1} - t_i$ indicates the duration of the window Wi (typically 100 ms). During the acquisition, it is recommended to separate the cables for the current injection and the voltage measurements (see Fig. 1b and Dahlin and Leroux, 2012). Such procedure minimizes two spurious effects. The first is related to electromagnetics capacitive and inductive couplings between the wires. The second is related to electrode polarization that prevents the current electrodes to be used as voltage electrodes for a certain amount of times (typically up to few minutes).

2.2. Forward and inverse modeling

In this section; we briefly recall the governing equations for the forward and inverse modeling performed in the present study. Readers can refer to Soueid Ahmed et al. (2018) for more details about the forward and inverse schemes used in Section 3 below. Generally speaking, the forward problem involves solving the following elliptic partial differential equation for the electric potential ψ (V):

$$-\nabla.(\sigma\nabla\psi) = \Im, \tag{2}$$

where σ(Sm^{-1}) denotes the electrical conductivity of the medium, and $\Im$ represents a volumetric source current term (A m^{-3}). In our case this term is given by the current injection at a given set of electrodes (typically the current I is injected at electrode A and retrieved at electrode B). Eq. (2) is used to compute the forward response of the medium (i.e., apparent or measured resistance and apparent or measured chargeability) as follows:

$$R_a = \frac{\Delta\psi}{I} \tag{3}$$

$$M_a = \frac{\Re(\sigma(1-M)) - \Re(\sigma)}{\Re(\sigma(1-M))} \tag{4}$$

where R_a (in Ohm) is the (apparent) resistance, $\Delta\psi$ (in V) is the electrical potential difference between two voltage electrodes M and N, and $M_a(-)$ is the apparent chargeability, $\Re$ is the forward operator defined in Eq. (2) and $M(-)$ is the intrinsic chargeability of the medium.

These quantities (i.e., R_a and M_a) can be used as input data in an inverse problem to obtain the spatial heterogeneities of the intrinsic parameters of the medium, i.e., the electrical conductivity and the chargeability distributions. All the unknowns can be collected in a model vector m. That said, we decoupled the conductivity and chargeability inverse problem by solving first the conductivity problem and then the chargeability problem. Solving such inverse problems can be formulated as an optimization in which a cost function is minimized. This cost function is written as the weighted sum of a data misfit term and a regularization term. The optimal solution could be found by using an iterative procedure. The inversion procedure we use below is discussed in Appendix A.

2.3. The dynamic Stern layer model

In order to interpret induced polarization tomograms, we need to describe a fundamental model developed in the past decade and called the dynamic Stern layer model (e.g., Revil, 2013). This model implies that most of the observed polarization in a metal-free porous material is due to the polarization of the Stern layer coating the surface of the grains. This Stern layer forms the inner part of the electrical double layer (the external part being the Gouy-Chapman diffuse layer). Considering that an external harmonic electric field $\mathbf{E} = \mathbf{E}_0\exp(+i\omega t)$ is applied to a porous material (the so-called primary field), the complex conductivity of the porous rock can be written as (Revil et al., 2017b)

$$\sigma^*(\omega) = \sigma_\infty - M_n\int_0^\infty \frac{h(\tau)}{1+(i\omega\tau)^{1/2}}d\tau + i\omega\varepsilon_\infty. \tag{5}$$

The quantity ω denotes the pulsation frequency (expressed in rad s^{-1}), ε_∞ is the permittivity of the material (in F m^{-1}), τ is a relaxation time (in s), and $h(\tau)$ denotes a (normalized) probability density for distribution of the time constants of the porous media. The normalized chargeability of the porous material is defined by,

$$M_n \equiv \sigma_\infty - \sigma_0, \tag{6}$$

where σ_∞ (S m^{-1}) defined the instantaneous conductivity of the material. This corresponds to the conductivity just after the application of the external (primary) electrical field. In this situation, all the charge carriers are mobile (see Fig. 2 in Revil et al., 2017a). The quantity σ_0 (S m^{-1}) defined the DC (Direct Current, i.e. steady-state) conductivity of the porous material. The DC conductivity is necessarily smaller than the instantaneous conductivity since the charges responsible for the polarization are not available anymore for the conduction process. Revil (2013) obtained the following expressions of the high and low frequency conductivities,

$$\sigma_\infty = \frac{{s_w}^n}{F}\sigma_w + \left(\frac{{s_w}^{n-1}}{F\phi}\right)\rho_g B\,\mathrm{CEC}, \tag{7}$$

$$\sigma_0 = \frac{{s_w}^n}{F}\sigma_w + \left(\frac{{s_w}^{n-1}}{F\phi}\right)\rho_g (B-\lambda)\mathrm{CEC}. \tag{8}$$

Eq. (7) to (8) leads to,

$$M_n = \left(\frac{{s_w}^{n-1}}{F\phi}\right)\rho_g\lambda\,\mathrm{CEC}. \tag{9}$$

The chargeability (a dimensionless quantity often expressed, however, in mV/V) is defined by $M = M_n/\sigma_\infty = (\sigma_\infty - \sigma_0)/\sigma_\infty$. In these equations, F (dimensionless) denotes the intrinsic formation factor related to the porosity ϕ (dimensionless) by the first Archie's law $F = \phi^{-m}$, m (dimensionless) is called the first Archie exponent or porosity exponent (Archie, 1942), n (dimensionless) is called the saturation exponent (dimensionless) and typically $m = n = 2$, s_w (dimensionless) denotes the water saturation θ related to the (volumetric) water content by $\theta = s_w\phi$, σ_w (in S m^{-1}) is the pore water conductivity, ρ_g denotes the grain density (in kg m^{-3}, usually $\rho_g = 2650$ kg m^{-3}), and CEC denotes the cation exchange capacity of the material. This cation exchange capacity corresponds to the density of exchangeable surface sites on the surface of the mineral grains. It is typically measured using titration experiments in which the surface of the grains is exchanged with a cation having a high affinity for the sites populating the mineral surface. It is expressed in C kg^{-1} or in meq/100 g with 1 meq/100 g = 963.20C kg^{-1}. In Eqs. (9) and (10), B (in m^2 s^{-1} V^{-1}) denotes the apparent mobility of the counterions for surface conduction and λ (in m^2 s^{-1} V^{-1}) denotes the apparent mobility of the counterions for the polarization associated with the quadrature conductivity. A dimensionless number R has been introduced by Revil et al. (2017b) R = λ/B. From our previous studies (e.g., Ghorbani et al., 2018), we have $B(\mathrm{Na}^+,\ 25\,^\circ\mathrm{C}) = 3.1 \pm 0.3\times10^{-9}\,\mathrm{m}^2\mathrm{s}^{-1}\mathrm{V}^{-1}$ and $\lambda(\mathrm{Na}^+,$

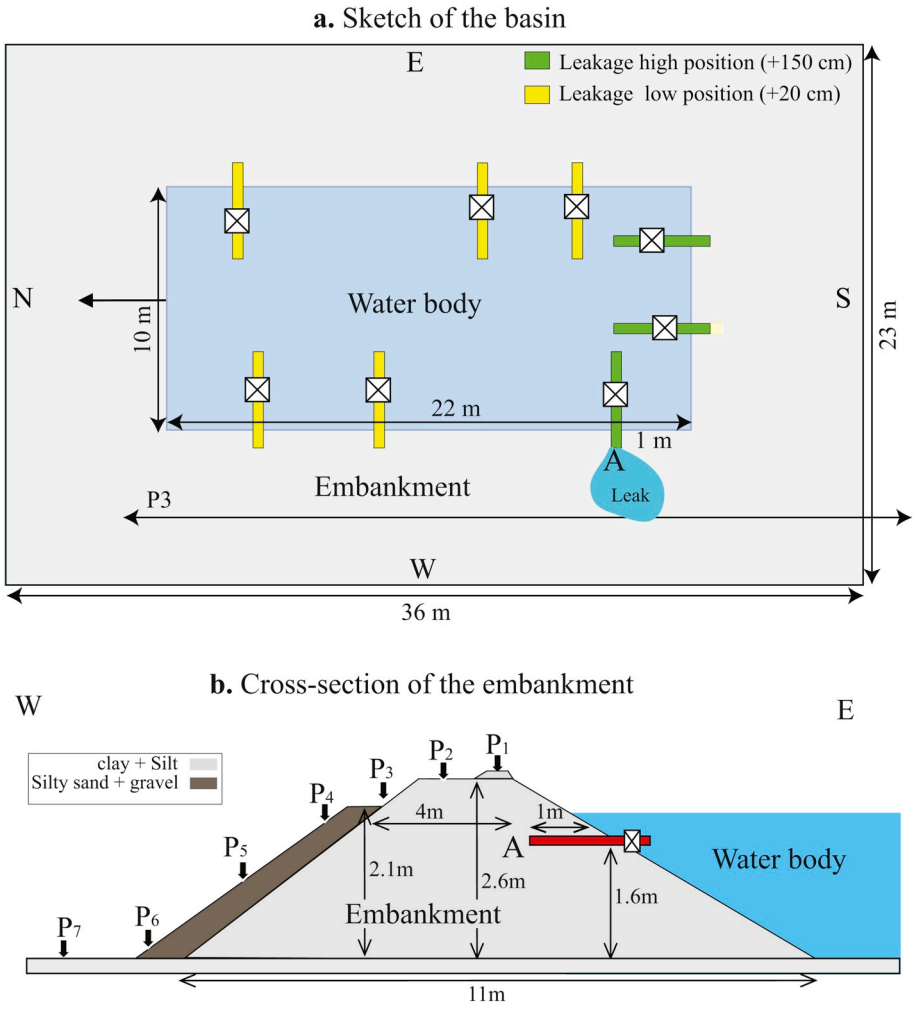


Fig. 2. Sketch of the experimental basin. (a) Up view of the basin. The central area in blue corresponds to the basin itself while the grey portion corresponds to the embankment. The valve used to generate the leak is located on the West-South area of the basin. Point A denotes the outlet of the pipe used for the leak. The position of the geophysical profile P3 (used for monitoring) is also shown. The high and low positions of the pipe are with respect to the bottom of the water reservoir. (b) Transverse cross section of the embankment, the location of the leakage source appears with the red tube. The relative location of the ERT and IP profiles (P1 to P7) on the outer side of the embankment. (For interpretation of the references to colour in this figure legend, the reader is referred to the web version of this article.)

25 °C) = 3.0 ± 0.7 × 10^{-10} $m^{-2}s^{-1}V^{-1}$, and R is typically around 0.09 ± 0.01 (Ghorbani et al., 2018).

In order to bridge time-domain and frequency-domain induced polarization, a quantitative relationship between the normalized chargeability and the quadrature conductivity is needed. Considering the quadrature conductivity at the geometric mean of two frequencies f_1 and f_2 and the normalized chargeability defined as the difference between the in-phase conductivity at frequency $f_2 > f_1$ and the in-phase conductivity at the lower frequency f_1, we have (Van Voorhis et al., 1973)

$$\sigma''(\sqrt{f_1 f_2}) \approx -\frac{M_n(f_1, f_2)}{\alpha}, \tag{10}$$

where α is given by:

$$\alpha \approx \frac{2}{\pi} \ln A, \tag{11}$$

and A denotes the number of decades separating high and low frequencies (for instance for two decades, i.e., $f_2 = 100 f_1$, $A = 10^2$).

Based on the previous petrophysical model and assuming $m = n$ (i.e., the cementation and saturation exponents are equal to each other), we can determine the water content from Eq. (9) as,

$$\theta = \left(\frac{M_n}{\rho_g \lambda \, \mathrm{CEC}} \right)^{1/(m-1)}, \tag{12}$$

where $\theta = s_w \phi$ denotes the water content and where CEC and m can be determined from petrophysical measurements. Since λ and ρ_g are well-determined constants, Eq. (12) requires only the measurement of the normalized chargeability and the knowledge of m. Assuming $m = 2$ (the default value for siliciclastic materials), the variation in the water content between two time t_1 and t_2 is given by,

$$\Delta\theta_{21} = \frac{M_n^2 - M_n^1}{\rho_g \lambda \, \mathrm{CEC}}. \tag{13}$$

With these equations, we can use the normalized chargeability tomograms to get the variations in the water content related to the occurrence of a leak in an embankment.

3. Test site

3.1. Site description

Our study was conducted over an experimental basin (Fig. 2) developed by IRSTEA (National Research Institute of Science and Technology for Environment and Agriculture) and located in the vicinity of Aix-en-Provence, in the Southern part of France. The dimension of the basin is 22 m of length and 10 m of width. The inner side of the basin filled with water is covered by a geomembrane. The geomembrane is protected by a geotextile and pavement on the inner sides. The embankment consists of homogeneous silt and clay materials. In addition, a thin layer of sands and gravels was placed on the outer side of the embankment to stabilize the structure (Fig. 2). The embankment is

made of a local red clay with a porosity of ~0.24 and a hydraulic conductivity of 10^{-9} m s^{-1} (both being average values).

The pipe buried in the embankment responsible for the leak is at a depth of 1.5 m below the crest of the embankment. In order to generate the leak, this pipe (see its outlet at position A in Fig. 2) was connected to a pressurized water supply and the fluid pressure was monitored during the duration of the leak (about 24 h). The flow rate was controlled through a valve, which can be opened at will. The water injected in the embankment has an electrical conductivity of 416 μS/cm at 22.5 °C, which was measured in the field. The flow rate is about 2.375 m^3/h with an upstream pressure equals to 162 kPa (recorded with a pressure transducer during the .experiment). The total volume of water injected into the embankment was 57 m^3. The experiment was conducted over a period of three days in July 2018. The weather before and during the experiment was hot and dry. Therefore, the water content in the embankment before the leak experiment was expected to be low.

3.2. Petrophysical measurements

Induced polarization is very sensitive to the variation of the water content as shown recently by the numerical experiment of Maineult et al. (2018) and various experimental data (e.g., Schmutz et al., 2012, and references therein). In order to get a rough idea of the properties of the red clay used for the embankment, a core sample was taken to get an idea of its electrical properties in the laboratory at ambient temperature. The undercompacted sample was saturated under vacuum and from its volume and mass at saturation, the porosity ϕ was found to be about 0.40 ± 0.01. The cation exchange capacity (CEC) measured with the cobalthexamine method (Aran et al., 2008; Ciesielski et al., 1997) was 20.1 meq/100 g, a pretty high value possibly indicating the presence of smectite in the clay fraction of this material.

Frequency-domain induced polarization measurements were performed between 10 mHz to 45 kHz using the ZELSIP04-V02 impedance meter built by Zimmermann et al. (2008) in Julich (Germany). The impedance meter and the sample holder are shown in Fig. 3. Three core samples were prepared and saturated with the same pore water as used in the field and at three distinct saturations (s_w = 1.0, 0.50 and 0.25 of saturation). The in-phase and quadrature conductivity spectra at these three saturations are shown in Fig. 4. In Fig. 5, we plot the normalized chargeability determined from the in-phase conductivity (using Eq. 8) as a function of the water content. From our laboratory measurements, we found that the normalized chargeability versus the water content can be fitted by a power law relationship with a cementation exponent $m = n = 3.1$. Such large value is consistent with the high value of the CEC as discussed in Revil et al. (1998). This result will be used below to interpret the normalized chargeability tomogram in terms of a variation in the water content.

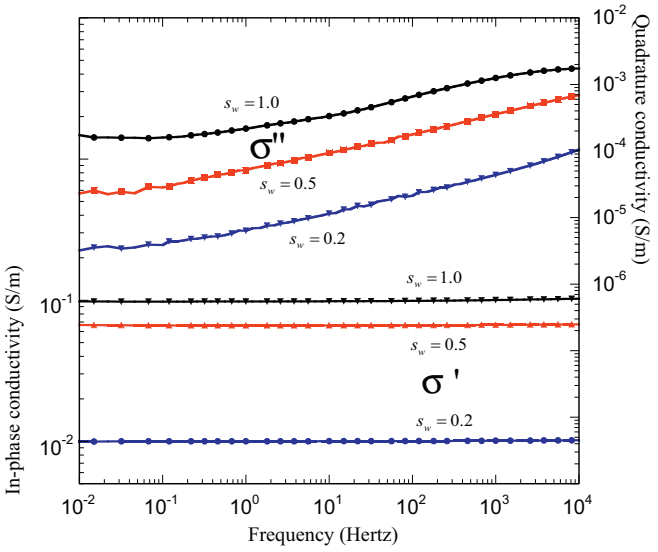


Fig. 4. Complex conductivity measurements of a core sample from the embankment. The measurements are performed at three water saturations. In-phase conductivity σ' (reflecting conduction) and quadrature conductivity σ'' (reflecting polarization) versus frequency. Note that both the in-phase and quadrature components are strongly sensitive to a change in the water content of the material. In this figure, the quantity s_w denotes the water saturation (ratio of the volume content of water by the porosity).

4. Field experiment

4.1. Conductivity and induced polarization survey

A total of 7 profiles parallel to each other were acquired in both conductivity and chargeability using an ABEM Terrameter SAS-4000 (ABEM Lund Imaging System) resistivity meter. The position of the profiles (labeled P1 to P7,) is shown in Fig. 2b. Each profile contains therefore 2 sets of 32 electrodes (one set to inject the current and one set to measure the potential, as shown in Fig. 1b). These two lines are separated by a distance of ~20 cm. Along each profile, the spacing between the electrodes is one-meter the distance between the profiles is 1.5 m. The multiple gradient array was used to acquire the data with a

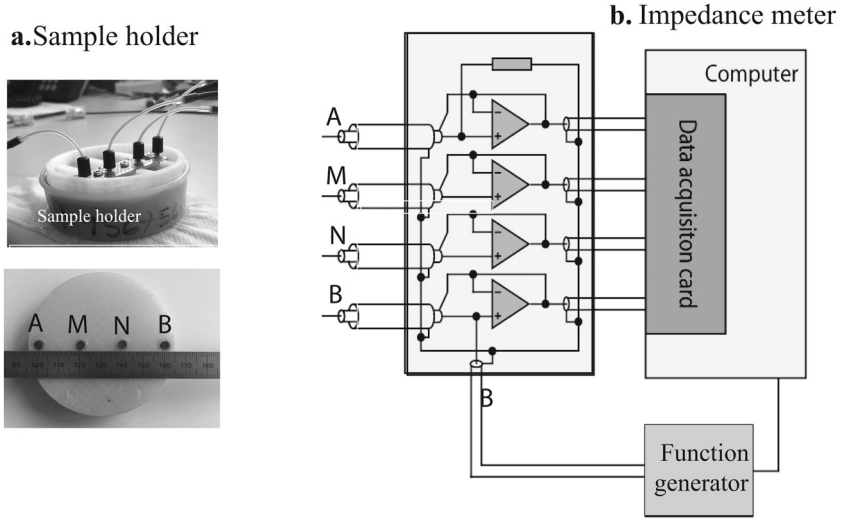


Fig. 3. Sample holder and impedance meter used for the laboratory experiment. (a) Picture of the sample holder with the 3D printed cover and picture of the cover with the encapsulated sintered electrodes. We used Ag/AgCl sintered electrode for the A, B, M, and N electrodes. (b) ZEL-SIP04-V02 impedance meter. This high precision impedance meter was built by Egon Zimmermann in Julich (Germany, see Zimmermann et al., 2008) and allows to measure the complex conductivity in the frequency range 1 mHz-45 kHz.

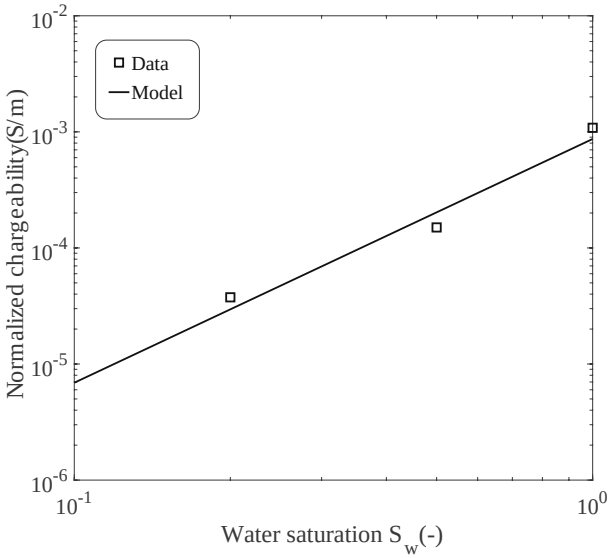


Fig. 5. Normalized chargeability as a function of the (water) saturation s_w. The plain line (model fit) corresponds to a power law fit of the data with Eq. (11). The fitted parameters are the saturation exponent ($n = 3.1$) and the normalized chargeability at saturation (8.5×10–$4\ \mathrm{S\,m^{-1}}$).

protocol comprising 224 quadrupoles per profile. Stainless steel electrodes were used for both current injection and voltage measurement.

The injected current is of the pseudo-continuous type ($+I$, 0, $-I$, 0) with one second of current injection and 1 s for measuring the secondary voltage decay. The current intensity was set to $I = 200$ mA. Ten partials chargeabilities were recorded during the monitoring time to get the total chargeability M. Typical apparent chargeability decay curves are shown in Fig. 6. As expected, we see the secondary voltages decaying quickly with time. Such decaying curves are usually expected in time-domain induced polarization. The 3D acquisition was performed before and during the leakage in order to image the variations in the water content of the subsurface. The mesh used for the forward and inverse modeling is shown in Fig. 7. In addition to the repeated survey, Profile P3 was used to perform a monitoring for the 3 days of the experiments (before, during and after the leak occurred). A total of 6 snapshots were acquired on this profile.

4.2. Self-potential survey

A self-potential survey was also performed at the ground surface over a surface area of 49 m^2 with a total of 8×8 stations. This survey was performed on the external side of the embankment and centered on the position of the leak and with a spacing of 1 m in the x and y directions. We used a pair of non-polarizable $Pb/PbCl_2$, NaCl electrodes to measure the potential differences between the reference electrode and the roving electrode. The reference electrode for the survey was placed remotely at about 20 m from the surveyed area. The measurements were performed with a high impedance voltmeter (100 MΩ) having a sensitivity of 0.1 mV. At each station, a small hole (~10 cm) was dug and filled with water-saturated bentonite and left few hours to get stabilized prior the measurements. This was done to ensure a repeatable electrical contact between the scanning electrode and the ground. The contact resistance measured at few stations was found to be good (around 2.5 kΩ). In order to check the drift in the electrode response, we repeated few measurements at each survey. One survey was done in < 10 min. Furthermore, the difference of electrical potential between both electrodes was checked by putting face-to-face the two electrodes before and after the measurement. It was stable at −1 mV.

5. Result and interpretation

5.1. 3D tomography

The two 3D tomograms of the electrical conductivity and chargeability before and during the leak are shown in Figs. 8 and 9. From these two tomograms, we can compute the normalized chargeability tomogram by multiplying, cell by cell, the conductivity by the chargeability. The normalized chargeability tomogram is shown in Fig. 10.

The three tomograms show that the structure of the embankment is quite homogenous in its center. The electrical conductivity tomogram shows that the embankment is quite conductive because of the presence of clays. The outer side of the embankment is less conductive because of the presence of the unsaturated sands and gravels placed on the external side of the embankment (see Fig. 2b). Downstream the positon of the pipe responsible for the leak, we observe clear changes in the tomograms. For instance, we notice that the amplitude of the normalized chargeability increases by more than one order of magnitude (from $0.001\ \mathrm{S\,m^{-1}}$ to $0.01\ \mathrm{S\,m^{-1}}$) in the area downstream the pipe (Fig. 10).

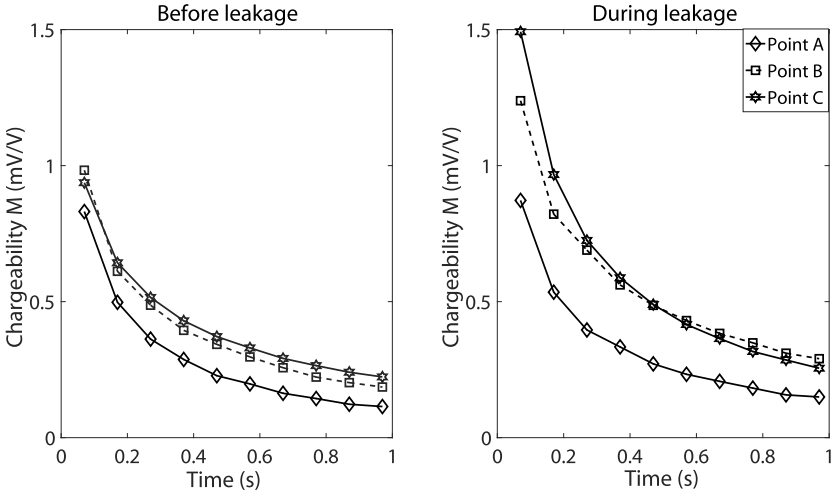


Fig. 6. Apparent chargeability decay curves recorded in the field on profile P3. The secondary voltage decay curves are measured on 10 windows, 0.1 s each. Only the first window is used for the inversion of the intrinsic chargeability. Point C is in the area of leakage close to the outlet while Point A is a remote point located far from the leak. Therefore it is logical that the apparent decay curve shows no variations in C while it shows a large variation in A.

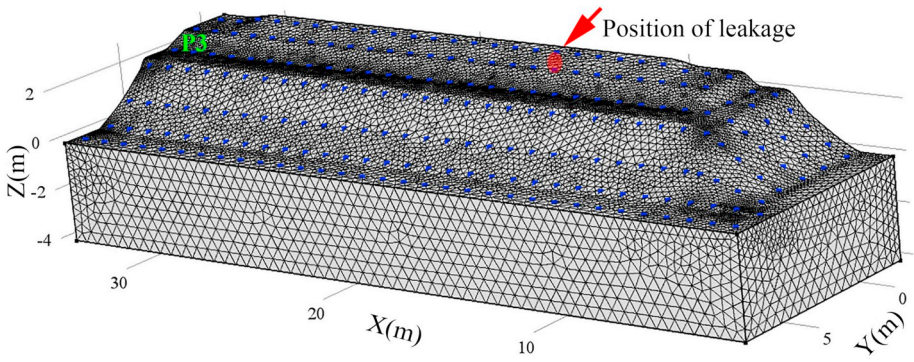


Fig. 7. Mesh used for the finite element forward modeling and inversion of the electrical conductivity and induced polarization data. It contains 39,251 elements. The blue points represent the position of the electrodes used for the 7 profiles labeled P1 to P7 (see Fig. 2b). The position of leakage is about 1.2 m below the red point at the ground surface. (For interpretation of the references to colour in this figure legend, the reader is referred to the web version of this article.)

Much smaller or no variations are shown elsewhere. This is consistent with what is shown in Fig. 5 using the core sample from the embankment. Using Eqs. (12) and (13), we can get a tomogram of the water content before and during the leakage. Fig. 11 shows the change in the water content distribution. It shows very clearly the ground water flow path followed by the leak.

In this study, the main source of electrical current measured with the self-potential method is the streaming current associated with the flow of the ground water. Indeed, the flow of the ground water drags the excess of electrical charges existing in the Gouy-Chapman diffuse layer coating the surface of the grains. The drag of this excess of charge corresponds by definition to a current source. Preferential flow paths in the shallow subsurface are generally associated with minima in the potential map obtained at the ground surface (Panthulu et al., 2001; Revil et al., 2004). In our survey, a self-potential map was first measured before leakage and this map (not shown here) was not displaying any specific anomaly that could have been interpreted as a preferential flow path. Few hours later and during the leakage, another survey shows a dramatic change (compared to the background response measured before leakage) in the electrical self-potential distribution. We notice the apparition of a connected path of small electrical potential values appearing in blue on the contour map shown in Fig. 12. There is a clear correlation between the pathway resulting from the interpretation of the self-potential data and the high values of the relative change in the water content resulting from the inversion of the induced polarization data (Fig. 12).

5.2. 2D monitoring

Profile P3 was used to carry out a monitoring of the electrical conductivity and normalized chargeability before, during and after the occurrence of the leak with a total of 6 snapshots realized. The acquisitions occur at the following elapsed times $t = -6$ h, $+21$ h, $+30$ h, $+33$ h, $+36$ h, and $+39$ h. The leak starts at $t = 0$ h (reference time) and

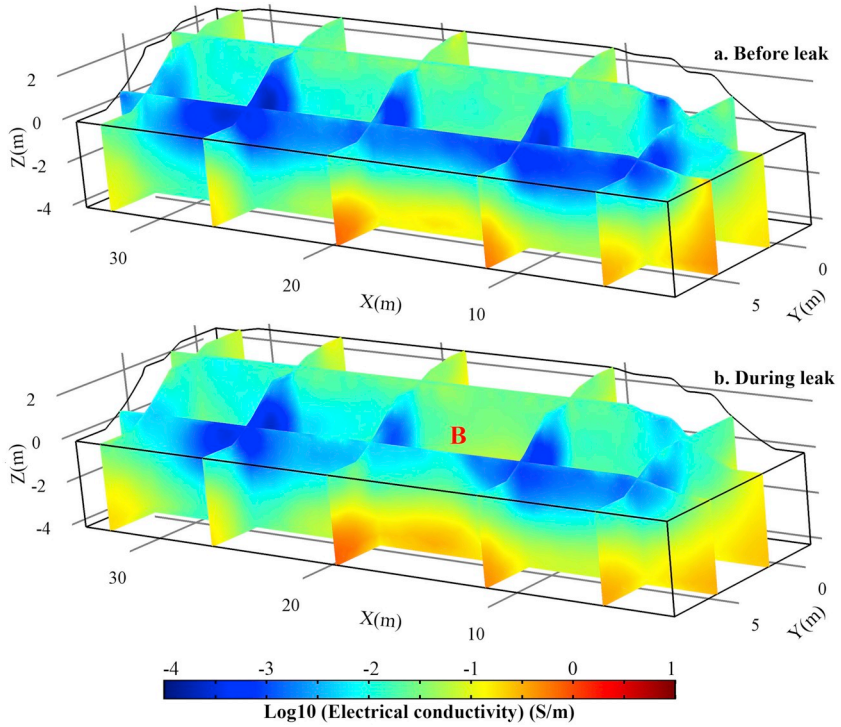


Fig. 8. 3D electrical conductivity tomogram. (a) Electrical conductivity tomogram obtained before the leakage. (b) Inverted electrical conductivity tomogram obtained during the leakage. The leak is visible in the 3D tomogram (see area B).

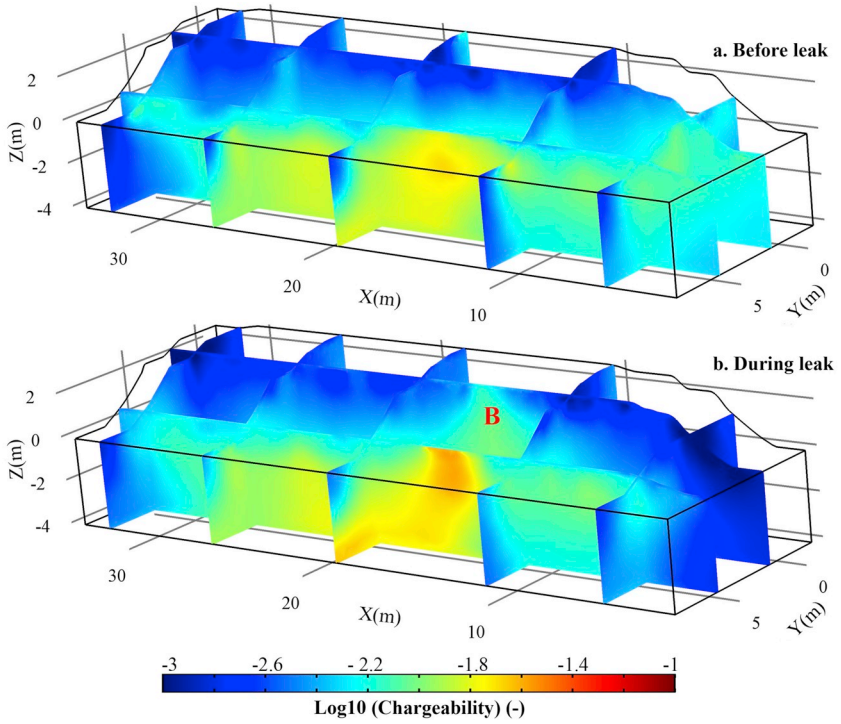


Fig. 9. 3D tomogram of chargeability. (a) This tomogram is realized with the data collected before the leak. (b) This second tomogram is realized with the data collected during the leak. An increase of the chargeability can be observed in the area labeled B.

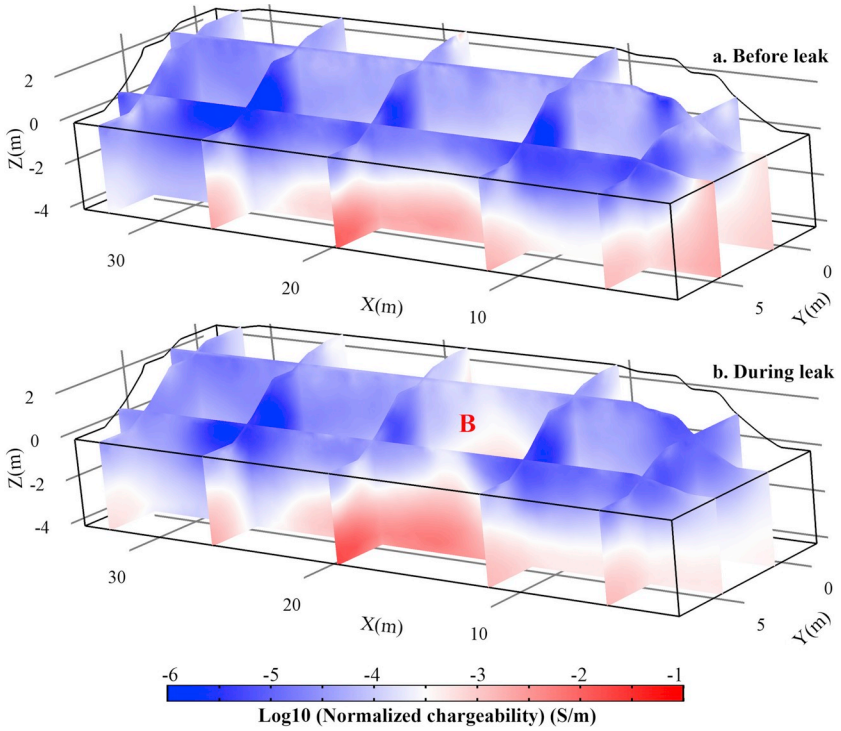


Fig. 10. Normalized chargeability (a) This tomogram is realized with the data collected before the leak. (b) This second tomogram is realized with the data collected during the leak. An increase of the normalized chargeability is observed in the area labeled B.

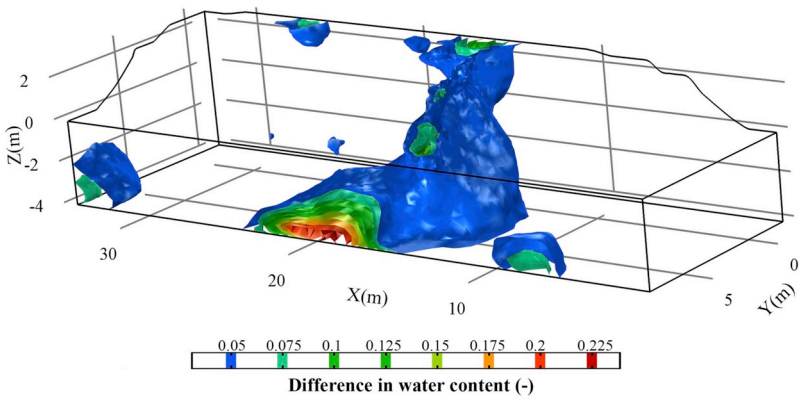


Fig. 11. Tomogram showing the variation in the water content underlying the preferential flow path of the ground water associated with the leak. We first determined the water content during and before the leakage from the normalized chargeability and then we substracted the two contributions to obtain this tomogram (see Eqs. 12 and 13). The tomogram shows very clearly that the anomaly originates at the outlet of the pipe used to generate the leak.

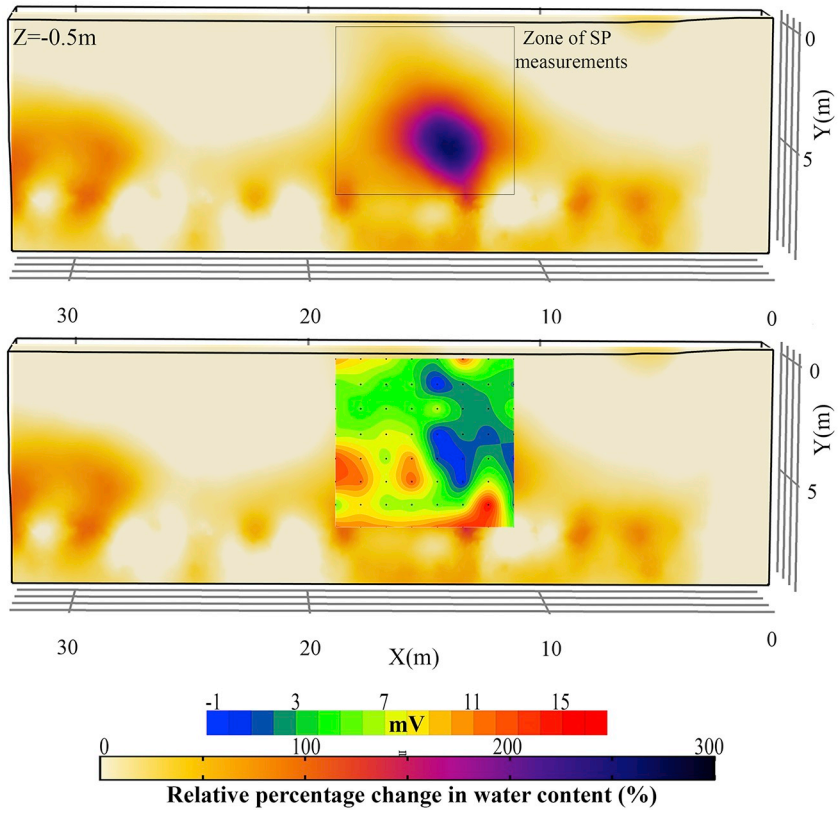


Fig. 12. Comparison between the relative variation of the water content at the shallow depth of 50 cm and comparison with the self-potential map from a survey realized 1 h after stopping leakage. The preferential flow path is expected to be associated with a negative self-potential anomaly (see modeling in Revil et al., 2017a, 2017b). Note that the orientation of the trend of negative values in the self-potential map is consistent with the trend depicted in Fig. 11.

ends at $t = +27$ h (h stands for hour and t for the elapsed time). Interestingly, some water starts to pond at the bottom of the embankment at $t = 3$ h. There are therefore 6 geophysical snapshots to invert.

The recorded data were inverted using the software developed in Kim (2009) and using a (3D + time) tomographic approach. We discretized the subsurface using tetrahedra. Each cell is assigned a conductivity and chargeability value. Using the finite-element approach, we model the conductivity and chargeability problems on the 2.5-D grid. The ground surface is assumed insulating and the normal component of the electrical field is therefore set to zero at the boundary. Topography is accounted for in the inversion. The calculation of the Jacobian matrix is based on the principles of reciprocity. The goal of time-lapse inversion is to determine the change in the resistivity and chargeability of each cell of the grid as a function of time. Karaoulis et al. (2011, 2013) developed an approach to invert the apparent resistivity and chargeability data looking for the optimum of several reference space models using the approximation that the material properties vary linearly in time between two subsequent reference models. Regularizations in both space domain and time domain is performed reducing inversion problems in presence of noisy data. The use of such time-lapse approach allows the simultaneous inversion of the different snapshots (6 in our case) in a single step. Then the data can be shown in terms of variations of the electrical conductivity or normalized chargeability by taking the logarithm of the ratio of the conductivity inverted data normalized by the conductivity of the reference tomogram.

Fig. 13 shows the variations in the electrical conductivity over the

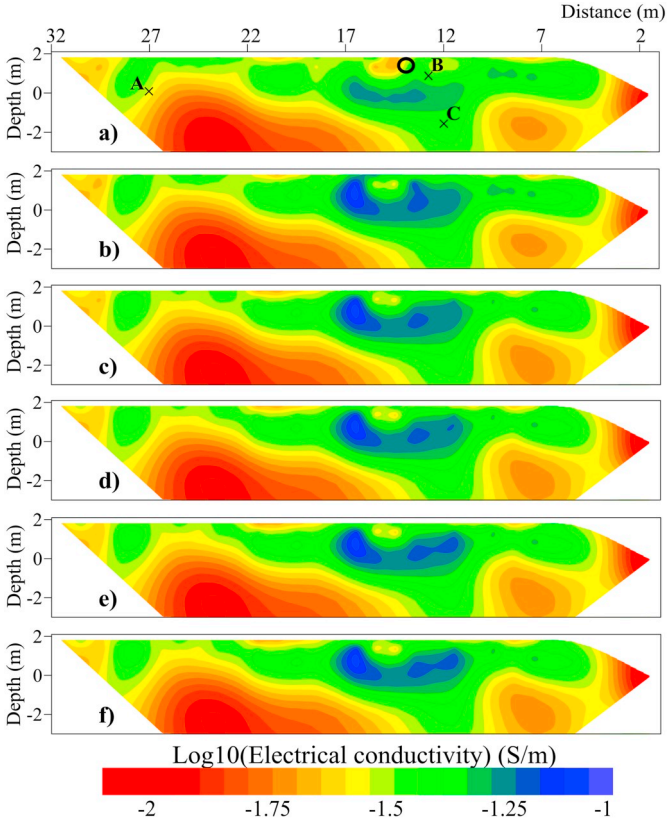


Fig. 13. Variation of electrical conductivity over time along a vertical cross-section along Profile P3. (a) Background conductivity prior the occurrence of the leak, which occurs at $t = 0$ h. The open circle denotes the projection of the outlet of the pipe. (b) to (f). Conductivity tomograms during and after the leakage. Note that the depth 0 m corresponds to the ground surface level at the bottom of the embankment. The area of leakage is the blue (conductive) area on the tomogram. The 6 snapshots correspond to the times $t = -6$ h, $+21$ h, $+30$ h, $+33$ h, $+36$ h, and $+39$ h, respectively. (For interpretation of the references to colour in this figure legend, the reader is referred to the web version of this article.)

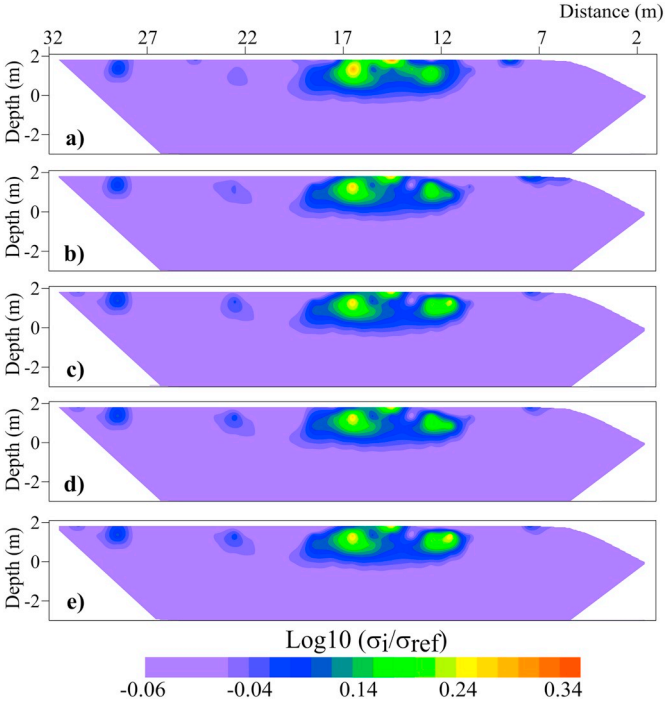


Fig. 14. Variation of electrical conductivity with respect to the reference profile taken prior the occurrence of the leak at $t = 0$ h. The changes in conductivity clearly underline two flow paths. Note that the depth 0 m corresponds to the ground surface level at the bottom of the embankment. So clearly the flow path below this profile is still confined inside the embankment. The 5 snapshots correspond to the time $t = +21$ h, $+30$ h, $+33$ h, $+36$ h, and $+39$ h, respectively.

duration of the experiment. From the inverted models, the electrical conductivity and normalized chargeability were picked up for three points (A, B, and C) from different depth levels and positions considering the position of the leak. The exact positions of A, B and C are shown on Fig. 13. In Fig. 14, we show the variations of the conductivity with respect to the reference conductivity tomogram taken prior the leak. We see clearly two distinct flow paths. The same work was done for the normalized chargeability.

Over the course of the experiment, points A and C (far from the leakage zone) show a negligible change on both M_n and σ_0 (Fig. 15). At the opposite, point B (located close to the outlet of the pipe) diplays considerable changes summarized by the increase of M_n and σ_0. This indicates clearly that induced polarization is an excellent method to monitor leakages in embankments dams and dikes. The change in magnitude of the normalized conductivity is compatible with the experimental data shown in Fig. 5 indicating a change in the saturation from 55% to 100% (fully saturated state). In order to combine the information on the conductivity and normalized chargeability tomography, we use a combination of scaled attributes. The target corresponds to the cells in which there is a concomitant increase of the conductivity and normalized chargeability. We write two attributes as

$$\eta_i^1 = \frac{\log_{10}\left(\frac{\sigma_i}{\sigma_{\text{Ref}}}\right)}{\text{Max}\left[\log_{10}\left(\frac{\sigma_i}{\sigma_{\text{Ref}}}\right)\right]}, \tag{14}$$

$$\eta_i^2 = \frac{\log_{10}\left(\frac{M_n^i}{M_{n,\text{Ref}}}\right)}{\text{Max}\left[\log_{10}\left(\frac{M_n^i}{M_{n,\text{Ref}}}\right)\right]}, \tag{15}$$

respectively, and where i denotes a given time. Then we combine the two attributes to define a leak index comprised between -1 and $+1$,

$$\eta = \eta_i^1 \eta_i^2. \tag{16}$$

In principle, since the tomograms have been normalized with respect to the reference profile acquired prior the leak, an increase of the water content should yield an increase of both the electrical conductivity and the normalized chargeability. Such concomitant increase of the conductivity and normalized chargeability are in turn associated with positive values the leak index η. Negative values would be associated with an increase of one of the two parameters and an decrease of the second one. This result would be unphysical with respect to what we know of the underlying physics described above in Section 2. A tomogram of the leak index is shown in Fig. 16. This tomogram shows clearly the area associated with the leakage downside the pipe. It is interesting to note that the area is confined to the embankment below profile P3. There is

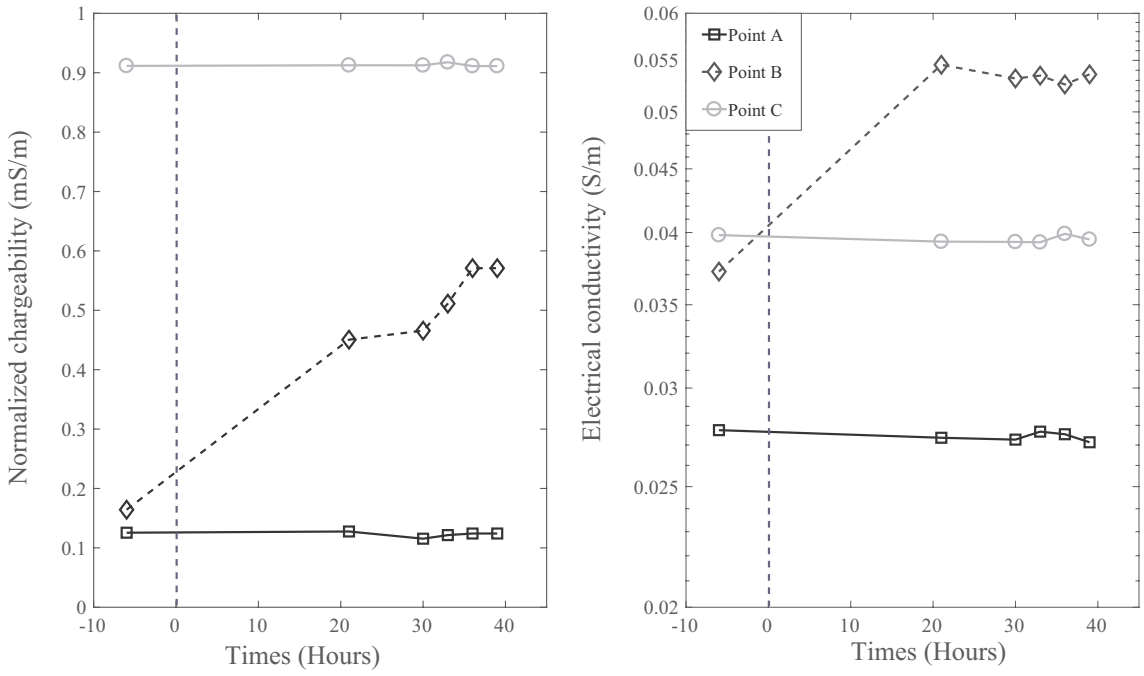


Fig. 15. Variation of the normalized chargeability (left) and electrical conductivity (right) at three points (A, B and C, positions shown in Figs. 13 and 14). The time t = 0 s denotes the start of the leakage.

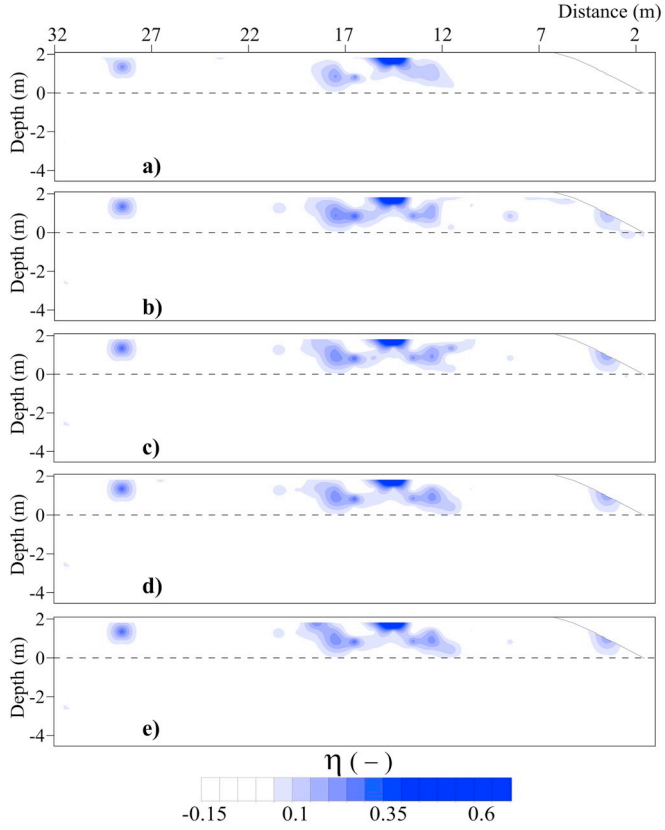


Fig. 16. Leakage index distribution computer below profile 3 (P3) resulting from the conductivity and normalized chargeability data. The dash line corresponds to the bottom of the embankment. We see that the flow is therefore confined to the embankment.

also a small anomaly at the beginning of the profile that remains unexplained.

6. Conclusion

Electrical conductivity of porous rocks and soils has two contributions. A bulk contribution associated with current flow through the pore network of the medium plus a surface conductivity associated with conduction in the electrical double layer coating the surface of the grains. Electrical resistivity tomography alone cannot allow separating these two contributions, which have different dependencies with the water content of the porous material. Induced polarization can be used to map another parameter, namely the normalized chargeability, which is directly proportional to the surface conductivity. Combining electrical resistivity tomography and induced polarization allows therefore separating the two contributions and therefore to obtain the water content without making any assumption regarding the amplitude of surface conductiivty with r.

Induced polarization tomography is applied for the first time to the detection of an artificial leakage created in the embankment of an experimental basin. 3D normalized chargeability tomography is used to image the change in the water content over time. Laboratory data using a core sample from the embankment demonstrates that the normalized chargeability follows a power law with the water saturation and therefore with the water content. This trend and the measured cation exchange capacity of the core sample are used to interpret the field data. The position of the flow path is also in agreement with independent self-potential measurements showing the position of the main flow path associated with the leak. A time-lapse survey performed on a single 2D profile normal to this pathway shows clearly the signature of the flow path in both the electrical conductivity and the normalized chargeability tomograms. A leak index is defined to combine the information content of the conductivity and normalized chargeability tomograms in order to visualize the leak. Induced

polarization is therefore a very promising method with huge implications in the monitoring of dams and embankments. Indeed, combining self-potential with induced polarization/conductivity surveys appear to be a good solution for which self-potential can be first used to identify potential leakage paths and then induced polarization/conductivity surveys can be used to estimate water content/saturation values.

Acknowledgements

This work was supported by the project RESBA ALCOTRA funded by the European Community. The postdoc of Abdellahi Soueid Ahmed is funded by EDF through a contract with the CNRS. We thank the Editor and one anonymous referee for their useful comments.

Appendix A. Tomography

The tomography is done with the Gauss-Newton method. The model vector **m** (conductivity or chargeability) is updated at each iteration k using:

$$\mathbf{m}_{k+1} = \mathbf{m}_k + \Delta\mathbf{m}_k, \tag{A1}$$

where the step Δm_k is computed through:

$$\Delta\mathbf{m}_k = [\mathbf{J}^T\mathbf{W}_d^T\mathbf{W}_d\mathbf{J} + \beta\mathbf{W}_m^T\mathbf{W}_m]^{-1}[\mathbf{J}^T\mathbf{W}_d^T\mathbf{W}_d(\mathbf{d} - F(\mathbf{m}_k)) - \beta\mathbf{W}_m^T\mathbf{W}_m\mathbf{m}_k] \tag{A2}$$

where **J** denotes the (sensitivity) Jacobian matrix, $\mathbf{W}_d$ is the data covariance matrix (taken here as a diagonal matrix weighting the data according to the measured standard deviation on the data), $\mathbf{W}_m$ is a roughening matrix entering the regularization function, **d** is the data vector (apparent resistivities and chargeabilities), and β is a parameter used to weight the two regularization terms in the cost function. In other words, we look for a smooth model of the subsurface conductivity or chargeability distributions that fits the observed data. Once the chargeability and conductivity distributions have been obtained, we can get a third quantity called the normalized chargeability. This quantity is obtained by multiplying in each cell the conductivity by the chargeability

References

Al-Saigh, H.N., Mohammed, S.Z., Dahham, S.M., 1994. Detection of water leakage from dams by self-potential method. Eng. Geol. 37 (2), 115–151. https://doi.org/10.1016/0013-7952(94)90046-9.

Aran, D., Maul, A., Masfaraud, J.-F., 2008. A spectrophotometric measurement of soil cation exchange capacity based on cobaltihexamine chloride absorbance. Compt. Rendus Geosci. 340 (12), 865–871. https://doi.org/10.1016/j.crte.2008.07.015.

Archie, G.E., 1942. The Electrical Resistivity Log as an Aid in Determining some Reservoir Characteristics. SPE-942054-G. https://doi.org/10.2118/942054-G.

Beck, Y.L., Ali Khan, A., Cunat, P., Guidoux, C., Artières, O., Mars, I.J., Fry, J.-J., 2010. Thermal monitoring of embankment dams by fiber optics. In: 8th ICOLD European Club Symposium, pp. 444–448. Innsbruck, Austria. https://hal.archives-ouvertes.fr/hal-00967826.

Binley, A., Kemna, A., 2005. DC resistivity and induced polarization methods. In: Rubin, Yoram, Hubbard, Susan S. (Eds.), Hydrogeophysics. Water Science and Technology Library 50 Springer, Netherlands, pp. 129–156. https://doi.org/10.1007/1-4020-3102-5_5.

Bolève, A., Revil, A., Janod, F., Mattiuzzo, J.L., Fry, J.-J., 2009. Preferential fluid flow pathways in embankment dams imaged by self-potential tomography. Near Surf. Geophys. 7 (5–6), 447–462. https://doi.org/10.3997/1873-0604.2009012.

Cardarelli, E., Cercato, M., De Donno, G., 2014. Characterization of an earth-filled dam through the combined use of electrical resistivity tomography, P- and SH-wave seismic tomography and surface wave data. J. Appl. Geophys. 106, 87–95. https://doi.org/10.1016/j.jappgeo.2014.04.007.

Ciesielski, H., Sterckeman, T., Santerne, M., Willery, J.P., 1997. Determination of cation exchange capacity and exchangeable cations in soils by means of cobalt hexamine trichloride. Effects of experimental conditions. Agronomie 17 (1), 1–7. https://doi.org/10.1051/agro:19970101.

Dahlin, T., Leroux, V., 2012. Improvement in time-domain induced polarization data quality with multi-electrode systems by separating current and potential cables. Near Surf. Geophys. 10 (6), 545–656. https://doi.org/10.3997/1873-0604.2012028.

Di Prinzio, M., Bittelli, M., Castellarin, A., Rossi Pisa, P., 2010. Application of GPR to the monitoring of river embankments. J. Appl. Geophys. 71 (2), 53–61. https://doi.org/10.1016/j.jappgeo.2010.04.002.

Fargier, Y., Lopes, P.S., Fauchard, C., François, D., Côte, P., 2014. DC-electrical resistivity imaging for embankment dike investigation: a 3D extended normalization approach. J. Appl. Geophys. 103, 245–256. https://doi.org/10.1016/j.jappgeo.2014.02.007.

Fauchard, C., Mériaux, P., 2007. Geophysical and geotechnical methods for diagnosing flood protection dikes: guide for implementation and interpretation. In: Edition Quae, ISBN 978-2_7542-0035-1. Paris. 124 pp.

Foster, M., Fell, R., Spannagle, M., 2000. The statistics of embankment dam failures and accidents. Can. Geotech. J. 37 (5), 1000–1024. https://doi.org/10.1139/t00-030.

Ghorbani, A., Revil, A., Coperey, A., Soueid Ahmed, A., Roque, S., Heap, M.J., et al., 2018. Complex conductivity of volcanic rocks and the geophysical mapping of alteration in volcanoes. J. Volcanol. Geotherm. Res. 357, 106–127. https://doi.org/10.1016/j.jvolgeores.2018.04.014.

Himi, M., Casado, I., Sendros, A., LoveraaL, R., Rivero, L., Casasa, A., 2018. Assessing preferential seepage and monitoring mortar injection through an earthen dam settled over a gypsiferous substrate using combined geophysical methods. Eng. Geol. 246, 212–221. https://doi.org/10.1016/j.enggeo.2018.10.002.

Ikard, S.J., Rittgers, J., Revil, A., Mooney, M.A., 2015. Geophysical investigation of seepage Beneath an Earthen Dam. Groundwater 53 (2), 238–250. https://doi.org/10.1111/gwat.12185.

Jessop, M., Jardani, A., Revil, A., Kofoed, V., 2018. Magnetometric resistivity: a new approach and its application to the detection of preferential flow paths in mine waste rock dumps. Geophys. J. Int. 215 (1), 222–239, 2018. https://doi.org/10.1093/gji/ggy275.

Karaoulis, M., Revil, A., Werkema, D.D., Minsley, B., Woodruff, W.F., Kemna, A., 2011. Time-lapse 3D inversion of complex conductivity data using an active time constrained (ATC) approach. Geophys. J. Int. 187, 237–251. https://doi.org/10.1111/j.1365-246X.2011.05156.x.

Karaoulis, M., Revil, A., Werkema, D.D., Tsourlos, P., Minsley, B.J., 2013. IP4DI: a software for time-lapse 2D/3D DC-resistivity and induced polarization tomography. Comput. Geosci. 54, 164–170.

Khan, A.A., Vrabie, V., Beck, Y.L., Mars, I.J., D'Urso, G., 2014. Monitoring and early detection of internal erosion: distributed sensing and processing. Struct. Health Monit. 1–15. https://doi.org/10.1177/1475921714532994.

Kim, J.H., 2009. DC2DPro-2D interpretation system of DC resistivity tomography. In: User's Manual and Theory. KIGAM, South Korea.

Lapenna, V., Binieris, K., Rizzo, E., et al., 2000. New prototype for 4D self-potential tomography in near-surface geophysical exploration. In: Nyguyen, C. (Ed.), Subsurface Sensing Technologies and Applications II. 4129 of Proceedings of SPIEpp. 447–456 San Diego, Calif, USA. July 2000.

Maineult, A., Jougnot, D., Revil, A., 2018. Variations of petrophysical properties and spectral induced polarization in response to drainage and imbibition: a study on a correlated random tube network. Geophys. J. Int. 212 (2), 1398–1411. https://doi.org/10.1093/gji/ggx474.

Martínez-Moreno, F.J., Delgado-Ramos, F., Galindo-Zaldívar, J., Martín-Rosales, W., López-Chicano, M., González-Castillo, L., 2018. Identification of leakage and potential areas for internal erosion combining ERT and IP techniques at the Negratín Dam left abutment (Granada, southern Spain). Eng. Geol. 240, 74–80. https://doi.org/10.1016/j.enggeo.2018.04.012.

Mendonça, C.A., 2008. Forward and inverse self-potential modeling in mineral exploration. Geophysics 73 (1), F33–F43.

Nzumotcha-Tchoumkam, L.A., Chouteau, M., Giroux, B., Rivard, P., 2010. A case study of self-potential detection of seepage at the junction of two embankment dams. In: Conference: Symposium on Application of Geophysics to Engineering and Environmental Problems (SAGEEP 2010), At Keystone, Colorado, USA, https://doi.org/10.4133/1.3445424. January 2010.

Panthulu, T.V., Krishnaiah, C., Shirke, J.M., 2001. Detection of seepage paths in Earth dams using self-potential and electrical resistivity methods. Eng. Geol. 59 (3), 281–295. https://doi.org/10.1016/S0013-7952(00)00082-X.

Perri, M.T., Boaga, J., Bersan, S., Cassiani, G., Cola, S., Deiana, R., Simonini, P., Patti, S., 2014. River embankment characterization: the joint use of geophysical and geotechnical techniques. J. Appl. Geophys. 11, 5–22. https://doi.org/10.1016/j.jappgeo.2014.08.012.

Peyras, L., Royet, P., Deroo, L., Albert, R., Becue, J.-P., Aigouy, S., Bourdarot, E., Loudiere, D., Kovarik, J.-B., 2008. French recommendations for limit-state analytical review of gravity dam stability. Eur. J. Environ. Civ. Eng. 12 (9–10), 1137–1164.

Revil, A., 2013. On charge accumulation in heterogeneous porous rocks under the influence of an external electric field. Geophysics 78 (4), D271–D291. https://doi.org/10.1190/geo2012-0503.1.

Revil, A., Florsch, N., 2010. Determination of permeability from spectral induced polarization in granular media. Geophys. J. Int. 181 (3), 1480–1498. https://doi.org/10.1111/j.1365-246X.2010.04573.x.

Revil, A., Cathles, L.M., Losh, S., Nunn, J.A., 1998. Electrical conductivity in shaly sands with geophysical applications. J. Geophys. Res. 103 (B10), 23 (925-23, 936).

Revil, A., Finizola, A., Sortino, F., Ripepe, M., 2004. Geophysical investigations at Stromboli volcano, Italy: implications for ground water flow and paroxysmal activity. Geophys. J. Int. 157 (1), 426–440. https://doi.org/10.1111/j.1365-246X.2004.

02181.x.
Revil, A., Cary, L., Fan, Q., Finizola, A., Trolard, F., 2005. Self-potential signals associated with preferential ground water flow pathways in a buried paleo-channel. Geophys. Res. Lett. 32 (7). https://doi.org/10.1029/2004GL022124.
Revil, A., Karaoulis, M., Johnson, T., Kemna, A., 2012. Review: some low-frequency electrical methods for subsurface characterization and monitoring in hydrogeology. Hydrogeol. J. 20 (4), 617–658. https://doi.org/10.1007/s10040-011-0819-x.
Revil, A., Kessouri, P., Torres-Verdín, C., 2014. Electrical conductivity, induced polarization, and permeability of the Fontainebleau sandstone. Geophysics 79 (5), D301–D318. https://doi.org/10.1190/GEO2014-0036.1.
Revil, A., Ahmed, A. Soueid, Jardani, A., 2017a. Self-potential: a non-intrusive ground water flow sensor. J. Environ. Eng. Geophys. 22 (3), 235–247. https://doi.org/10.2113/JEEG22.3.235.
Revil, A., Coperey, A., Shao, Z., Florsch, F., Fabricius, L.I., Deng, Y., Delsman, J.R., 2017b. Complex conductivity of soils. Water Resour. Res. 53 (8), 7121–7147. https://doi.org/10.1002/2017WR020655.
Rittgers, J.B., Revil, A., Karaoulis, M., Mooney, M.A., Slater, L.D., Atekwana, E.A., 2013. Self-potential signals generated by the corrosion of buried metallic objects with application to contaminant plumes. Geophysics 78 (5), EN65–EN82. https://doi.org/10.1190/GEO2013-0033.1. (2013).
Schmutz, M., Blondel, A., Revil, A., 2012. Saturation dependence of the quadrature conductivity of oil-bearing sands. Geophys. Res. Lett. 39, L03402. https://doi.org/10.1029/2011GL050474.
Soueid Ahmed, A., Revil, A., 2018. 3-D time-domain induced polarization tomography: a new approach based on a source current density formulation. Geophys. J. Int. 213 (1), 244–260. https://doi.org/10.1093/gji/ggx547.
Soueid Ahmed, A., Revil, A., Byrdina, S., Coperey, A., Gailler, L., Grobbe, N., Viveiros, F., 2018. 3D electrical conductivity tomography of volcanoes. J. Volcanol. Geotherm. Res. 356, 243–263. https://doi.org/10.1016/j.jvolgeores.2018.03.017.
Titov, K., Tarasov, A., Ilyin, Y., Seleznev, N., Boyd, A., 2010. Relationships between induced polarization relaxation time and hydraulic properties of sandstone. Geophys. J. Int. 180 (3), 1095–1106. https://doi.org/10.1111/j.1365-246X.2009.04465.x.
Van Voorhis, G.D., Nelson, P.H., Drake, T.L., 1973. Complex resistivity spectra of porphyry copper mineralization. Geophysics 38 (1), 49–60. https://doi.org/10.1190/1.1440333.
Vinegar, H., Waxman, M., 1984. Induced polarization of shaly sands. Geophysics 49 (8), 1267–1287. https://doi.org/10.1190/1.1441755.
Zimmermann, E., Kemna, A., Berwix, J., Glaas, W., Münch, H.M., Huisman, J.A., 2008. A high-accuracy impedance spectrometer for measuring sediments with low polarizability. Meas. Sci. Technol. 19 (10), 105603. https://doi.org/10.1088/0957-0233/19/10/105603.